Delft University of Technology

Measuring phase and polarization singularities of light using spin-multiplexing metasurfaces

Fu, Yanan; Min, Changjun; Yu, Jiahao; Xie, Zhenwei; Si, Guangyuan; Wang, Xianyou; Zhang, Yuquan; Lei, Ting; Urbach, H. P.; More Authors

Important note
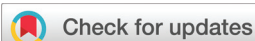To cite this publication, please use the final published version (if applicable).
Please check the document version above.

Nanoscale

Measuring phase and polarization singularities of light using spin-multiplexing metasurfaces†

Yanan Fu,‡[a] Changjun Min,‡[a] Jiahao Yu,[a] Zhenwei Xie,[a] Guangyuan Si,[b] Xianyou Wang,[a] Yuquan Zhang, [ID] *[a] Ting Lei,[a] Jiao Lin,[a,b,c] Dapeng Wang,[a] H. P. Urbach[d] and Xiaocong Yuan*[a]

In recent years, light beams containing phase or polarization singularities, such as optical vortices (OVs) and cylindrical vector beams (CVBs), have contributed to significant applications including optical orbital angular momentum (OAM) communications, particle trapping and manipulation, and super-resolved imaging. However, traditional methods for detecting the phase and polarization singularities of light suffer from drawbacks, such as large device size, complicated optics, and limits in detection function. Here, we propose an alternative method for detecting simultaneously phase and polarization singularities based on a spin-multiplexing metasurface. Both numerical and experimental results demonstrate that the metasurface device can be used to measure accurately the topological charge of OVs and the polarization order of CVBs individually or simultaneously, and exhibit beneficial attributes such as a broadband response, compactness, and system simplification. This method offers great potential in applications such as singular optical beam shaping and high-capacity OAM/CVB multiplexing communication.

1. Introduction

As a branch of modern optics, singular optics has attracted broad research interest over the past decades.[1,2] Two typical optical singularities, phase and polarization singularities originating from the uncertainty in the phase or polarization in the optical field, have been investigated in depth and widely applied in various optical fields, including imaging and metrology,[3] atom optics,[4] nonlinear optics,[5] optical tweezers,[6] optical sensing,[7] quantum optics and information,[8,9] and optical communications.[10,11]

The concept of phase singularity was first proposed and experimentally confirmed by Nye and Berry and colleagues in the 1970s.[12] As a typical beam with phase singularity, the optical vortex (OV) has been studied widely because of its special optical properties such as its spiral phase wavefront $\exp(il\theta)$, orbital angular momentum (OAM),[13] and zero inten-

sity in the center of the beam. Based on these properties, the OV has been employed in many interesting applications in recent years. For instance, because OV beams with different OAMs are orthogonal and the topological charge l of OAMs can in theory take arbitrary integer values, OAM-multiplexing has proved to enhance the information capacity of optical communication systems in both free space and optical fibers.[10,11,14] The rotational torque generated by OAMs has been effectively applied in optical tweezers to trap and rotate micro- and nano-particles.[15] The donut-shaped intensity pattern and tunable spiral phase of the OV has been used in the excitation of surface plasmon polaritons (SPPs), and in structured illumination microscopy imaging.[16]

A representative beam with a polarization singularity is a cylindrical vector beam (CVB),[17] which can be expressed as a set of characteristic solutions of Maxwell's equation cast in cylindrical coordinates. The CVB also has a donut-shaped intensity pattern because of the singularity in polarization at the center of the beam and shows locally linear polarization at each point in the beam's cross section but with space-dependent orientations. Two famous examples of CVBs are the radially polarized beam and the azimuthally polarized beam, for which the polarization orientations at each point in the beam cross section are all along the radial and azimuthal directions, respectively.[18] Because of the vector nature of the CVB, especially for focusing conditions with high numerical aperture (NA), various unique focal field distributions can be generated by CVBs, such as sub-wavelength focal spots,[19]

[a]*Nanophotonics Research Center, Shenzhen Key Laboratory of Micro-Scale Optical Information Technology, Shenzhen University, Shenzhen 518060, China. E-mail: xcyuan@szu.edu.cn, yqzhang@szu.edu.cn*

[b]*Melbourne Centre for Nanofabrication, Australian National Fabrication Facility, Clayton, VIC 3168, Australia*

[c]*School of Engineering, RMIT University, Melbourne, Victoria 3001, Australia*

[d]*Optics Research Group, Delft University of Technology, Lorentzweg 1, 2628CJ Delft, The Netherlands*

longitudinal optical needles,[20] multiple focal spots,[21] and spin–orbital angular momentum coupling,[22] all of which are contributing to many promising applications. For example, with the orthogonality of CVBs with different orders,[17] it has been widely used in CVB-multiplexing communications.[23]

Besides the OV and CVB with only one singularity in the phase or polarization, a light beam can contain both phase and polarization singularities, for example, the cylindrical vortex vector beam (CVVB).[18] This beam has both a spiral wavefront and a vectorial polarization distribution, offering more degrees of freedom for optical field modulation and multiplexing.[24]

To explore other applications of singular optical beams, detection methods for these optical singularities need to be developed, especially the OAM of OVs and the polarization order of CVBs. For OAM detection, previous methods are based on traditional optical diffraction or interference devices, such as the diffraction grating, spatial light modulator, and Mach–Zehnder interferometer.[25] Conventional methods for detecting polarization singularities usually involve space-variant half-wave plates and polarizers[26] or diffraction gratings.[27] However, these detection methods have drawbacks such as requiring multiple devices, large optical systems, complex detection processes, and low diffraction efficiencies that strongly limit their applications in some new compact optical systems with optical fibers or integrated chips.

In recent years, metasurface devices were proposed to significantly improve the performance of traditional optical devices.[28,29] Metasurfaces have characteristics such as compact device size (micron scale), thin thicknesses (nanoscale), broadband responses (visible to infrared), high efficiency (more than 80%), and multi-functional characteristics (multi-parameter control of light). They therefore have become of topical interest[30] inspiring other methods of optical singularity detection. For example, self-interference using a plasmonic metasurface was designed for OAM detection,[31] and combined elements based on the Pancharatnam–Berry phase were studied for CVB detection.[32] However, most previous metasurface-based detection methods respond only to either the phase singularity or the polarization singularity, and some methods require multiple metasurface devices to work together.[32] Thus, it is still a task of challenge to detect both phase and polarization singularities of light with the same compact device.

In this paper, we propose and experimentally demonstrate an alternative method for detecting phase and polarization singularities simultaneously based on a designed single spin-multiplexing metasurface. The metasurface is composed of a plasmonic semi-ring aperture array with a detour phase distribution on a metal film. Because the photonic spin–orbit angular momentum conversion is induced by the plasmonic semicircular aperture, and the continuous geometric phase gradient is generated by the semicircular aperture, the metasurface therefore works as a spin-multiplexing device. The spatial distribution of semi-circular apertures is designed employing the detour-phase principle to generate two 3 × 3 OV arrays with different OAMs in the far field for the two spin

states (left- or right-circular polarization), respectively. Based on such metasurface devices, the topological charge of the OV and the polarization order of the CVB can be measured individually or simultaneously by detecting the position of the restored Gaussian point in the far-field OV arrays. Our experimental results agree well with the theoretical predictions, proving that the proposed method is efficient in detecting both the phase and polarization singularities of light. Moreover, three different wavelengths of 473 nm, 532 nm, and 633 nm are chosen in the experiment to demonstrate its broadband response feature.

2. Detecting the principle of phase and polarization singularities

Here, the detecting principle of both phase and polarization singularities is based on a spin-multiplexing metasurface, which may achieve different phase modulations for left- and right-circular polarized beams. In the working principle of the metasurface (Fig. 1), when a circularly polarized light is normally incident on the metasurface, the output beam propagates to the left or right direction depending on its spin state, just like a spin-dependent beam splitter. In our design, the right/left circularly polarized (R/LCP) light propagates to the left/right side (Fig. 1a). Then, the left- or right-side output beam generates respectively a far-field OV array with different OAMs due to the phase modulation of the metasurface. If the incident circularly polarized light has a spiral wave front with OAM, the specific position of the OV array is restored to a bright Gaussian point depending on the OAM value of incident light, but all other positions of the OV array maintain a
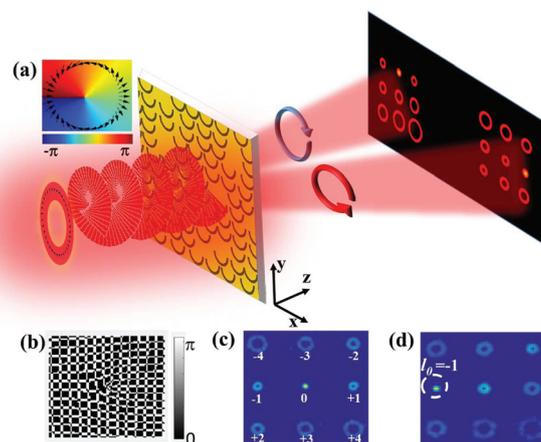

Fig. 1 (a) Schematic illustration for detecting both phase and polarization singularities based on the spin-multiplexing metasurface. The blue (red) circular arrow indicates a right (left) circularly polarized beam. Inset at top left—phase and polarization distribution of incident light (the polarization distribution is described by black arrows); (b) binary phase distribution of the DOVG for a 3 × 3 OV array; (c) simulated OV array distribution in the far field; (d) schematic illustration of phase singularity detection for an incident OV with l = 1.

donut-shaped pattern with a dark center. Hence, the OAM of the incident light is detected through the metasurface depending on the position of the restored Gaussian point.

To generate the OV array for phase singularity detection, we need to control the phase distribution of the metasurface based on the principle of a two-dimensional Dammann optical vortex grating (DOVG)[33] for which the phase distribution of the binary phase $\Phi(x, y)$ satisfies the following expression[34]

$$
\exp[i\Phi(x,y)] = \\
\sum_{N=-\infty}^{+\infty} \sum_{M=-\infty}^{+\infty} a_{MN} \exp\left[iM\left(\frac{2\pi x}{d_x} + \Delta l_x \theta\right) + iN\left(\frac{2\pi y}{d_y} + \Delta l_y \theta\right)\right]
\tag{1}
$$

where $|a_{mn}|^2$ is the energy of each diffraction order normalized to the total power, d_x and d_y are the grating periods in the x and y directions, respectively, and angle θ is defined using $\theta = \arctan(y/x)$. Δl_x and Δl_y are the intervals of the topological charge in x and y directions, respectively. Another advantage of the DOVG is that the energy of each OV in the generated OV array can be modulated to equal the value of $|a_{mn}|^2$. Based on the phase distribution of the DOVG, a beam without OAM incident on the DOVG is diffracted into $M \times N$ orders, each with equal energy carrying topological charge $l_0 = M\Delta l_x + N\Delta l_y$. Fig. 1b gives an example of the DOVG phase distribution for generating a 3 × 3 OV array with $\Delta l_x = 1$ and $\Delta l_y = -3$. When a Gaussian light beam without OAM is normally incident on the metasurface with phase distribution of the DOVG, the desired 3 × 3 OV array with uniform energy and different topological charges ranging from $l_0 = -4$ to $+4$ are generated (Fig. 1c). When a beam with topological charge l is incident on the DOVG, the beam can be diffracted into $M \times N$ orders, which can be described as:

$$
\exp[i\Phi(x,y)'] \\
= \sum_{N=-\infty}^{+\infty} \sum_{M=-\infty}^{+\infty} a_{MN} \exp\left[iM\left(\frac{2\pi x}{d_x} + \Delta l_x \theta\right) + iN\left(\frac{2\pi y}{d_y} + \Delta l_y \theta\right) + il\theta\right] \\
= \sum_{N=-\infty}^{+\infty} \sum_{M=-\infty}^{+\infty} a_{MN} \exp\left[iM\frac{2\pi x}{d_x} + iN\frac{2\pi y}{d_y} + iM\Delta l_x \theta + iN\Delta l_y \theta + il\theta\right] \\
= \sum_{N=-\infty}^{+\infty} \sum_{M=-\infty}^{+\infty} a_{MN} \exp\left[iM\frac{2\pi x}{d_x} + iN\frac{2\pi y}{d_y} + i(l_0 + l)\theta\right]
\tag{2}
$$

the topological charges of the generated OV array are modulated to give $l' = l + l_0$. If the incident light is an OV beam with topological charge $l = +1$, then the position in the OV array with $l_0 = -1$ is restored to a bright Gaussian point ($l' = 0$) for OAM detection (Fig. 1d). The restored Gaussian point appears on either the left or the right side of the far-field OV array depending on the spin state of the incident light (Fig. 1), demonstrating that the metasurface device detects both the spin angular momentum (SAM) and OAM of the incident light.

Next, we describe how to detect the polarization singularity of CVBs. The polarization state of the mth-order CVB is defined by the Jones vector J_m,[32]

$$
J_m = \begin{pmatrix} \cos(m\varphi + \phi_0) \\ \sin(m\varphi + \phi_0) \end{pmatrix} = \begin{pmatrix} \frac{1}{2}\left\{e^{i(m\varphi+\phi_0)} + e^{-i(m\varphi+\phi_0)}\right\} \\ \frac{1}{2i}\left\{e^{i(m\varphi+\phi_0)} - e^{-i(m\varphi+\phi_0)}\right\} \end{pmatrix} \\
= \frac{1}{2}e^{i(m\varphi+\phi_0)}\begin{pmatrix} 1 \\ -i \end{pmatrix} + \frac{1}{2}e^{-i(m\varphi+\phi_0)}\begin{pmatrix} 1 \\ i \end{pmatrix}
\tag{3}
$$

where m is the polarization order, φ is the azimuthal angle, and φ_0 is the initial phase angle. From eqn (3), the mth-order CVB decomposes into a pair of conjugated OV beams, including a right circularly polarized OV with topological charge $l = m$ and a left circularly polarized OV with topological charge $l = -m$, so the detection of the polarization order of CVBs is converted to the detection of the topological charges of the two decomposed OV beams. That is, when a m_{th}-order CVB is normally incident on the metasurface, two output beams of opposite spin states propagate to the left and right side, respectively, and then form two OV arrays with restored Gaussian points at positions $l_0 = -m$ and $l_0 = m$, respectively. Because the two Gaussian points are restored at the conjugated positions, then the polarization order m of the CVB can be determined from the position of either Gaussian point.

Besides the OV and CVB, the CVVB with both phase and polarization singularities can also be detected by the metasurface. Similarly, the Jones vector of a CVVB with topological charge l and polarization order m is simply defined by,

$$
J_{l,m} = e^{il\varphi}\begin{pmatrix} \cos(m\varphi + \phi_0) \\ \sin(m\varphi + \phi_0) \end{pmatrix} \\
= \frac{1}{2}e^{i((l+m)\varphi+\phi_0)}\begin{pmatrix} 1 \\ -i \end{pmatrix} + \frac{1}{2}e^{-i((m-l)\varphi+\phi_0)}\begin{pmatrix} 1 \\ i \end{pmatrix}
\tag{4}
$$

where φ is the azimuthal angle, and φ_0 is the initial phase angle. Similarly for a CVB, we find that from eqn (4), a CVVB also decomposes into a pair of OV beams, including a right (left) circularly polarized OV with topological charge $l + m$ ($l - m$), and therefore also generates two OV arrays in the far field *via* the metasurface. From the detection principle of the OV and CVB, the position of $l_0 = -(l + m)$ on the left-side OV array and the position $l_0 = -(l - m)$ on the right-side OV array is restored to the Gaussian points. Therefore, we can determine the values of $l + m$ and $l - m$ depending on the positions of the two Gaussian points, and finally calculate the values of l and m in the detection of both phase and polarization singularities.

3. Design of the spin-multiplexing metasurface

To achieve the above-mentioned detection functions, we need a metasurface device that can generate two OV arrays for the LCP and RCP light, respectively. Note that several previously reported spin-multiplexing metasurfaces may be chosen to achieve these goals.[35] Based on our fabrication conditions, we designed a new spin-multiplexing metasurface composed of a plasmonic semi-ring aperture array with a detour phase distribution (Fig. 2a) and demonstrated that it can serve as an
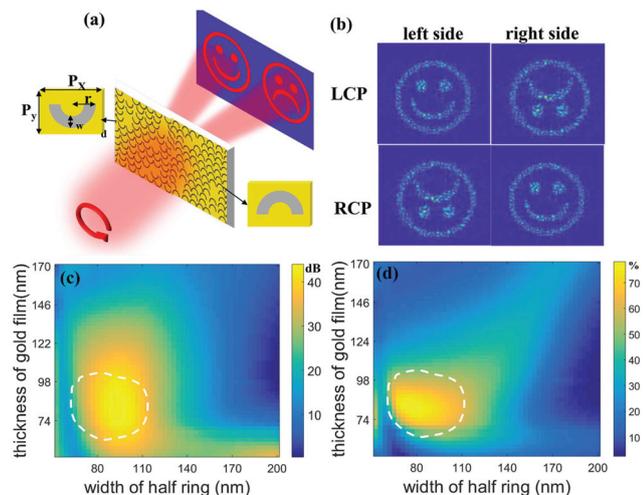
Fig. 2 (a) Schematic illustration of the principle of the multiplexing metasurface. The enlarged unit cell shows that it is composed of two semi-ring apertures with opposite orientations. When a LCP light is incident on the metasurface, the happy and sad faces are reconstructed on the left and right region of the far field, respectively; (b) FDTD simulation results of the spin-multiplexing performance. The first (second) line shows the result under illumination of the LCP/RCP light. The structural parameters used in the FDTD simulation are: P_x = 0.896 μm, P_y = 0.45 μm, r = 0.37 μm, w = 0.07 μm, and d = 0.1 μm; dependence of (c) polarization extinction ratio and (d) efficiency with thickness d of the gold film and the width w of the semi-ring aperture at the wavelength of 633 nm; here, the efficiency is defined as the energy of the desired pattern divided by the total energy passing through the metasurface.

efficient spin-multiplexing metasurface. We combined two kinds of semi-ring apertures to generate two different patterns at one circular polarized light incidence, and once the spin of incident light changed, the position of the two patterns in the far field will be exchanged.

The unit structure of the metasurface (inset of Fig. 2a) comprises a plasmonic semi-ring aperture in a metal film. Similar to some previous reports,[36] the photonic spin–orbit interaction[37] in this aperture induces an opposite phase gradient for the LCP and RCP light. Therefore, when LCP or RCP light passes through an array of the proposed semi-ring aperture, they are deflected into two opposite directions depending on the spin state, and hence they show the desired spin-multiplexing function, details of the spin response of the unit cell can be found in ESI Fig. S1.† Note that there are two opposite types of semi-ring apertures, similar to the upper and lower halves of a circle (the two insets of Fig. 2a), which induce opposite phase gradients and used together to generate different far-field patterns on the left and right sides. Referring to Fig. 2a, when a LCP light is incident on the metasurface, one type of semi-ring aperture in the metasurface deflects the light to the left side and forms a "happy face" pattern, whereas the other type deflects the light to the right side and forms a "sad face" pattern. In Fig. 2b, we show the corresponding finite-difference time-domain (FDTD) simulation results for the left and right circularly polarized light. They agree well with expectations (Fig. 2a).

The happy- and sad-face patterns (Fig. 2b) are generated by the metasurface with a holographic phase distribution that depends on the detour-phase principle, which has been applied in several previous meta-hologram devices.[38–40] Here, we built the desired two-dimensional phase distribution $\varphi(i,j)$ of the metasurface by changing all the semi-ring positions in the unit cell based on the detour-phase principle. In our design, we define the central position of the unit cell as $\varphi(i,j) = 0$. We then obtain a $\varphi(i,j)$ varying from $-\pi$ to $+\pi$ when the position of the semi-ring aperture moves from the left to right border of the unit cell, to finally form the desired phase profile of the hologram. Details of the detour phase principle can be found in ESI Fig. S2.† Note that the phase changes induced by plasmonic resonance inside the semi-ring aperture are not taken into consideration here, as the metal film is thin (100 nm) and all unit cells are the same. The Gerchberg–Saxton algorithm is used to optimize the phase profiles of the happy and sad face patterns.[41]

To investigate the influence of structural parameters on the performance of designed metasurfaces (Fig. 2c and d), we show the FDTD results of the efficiency and polarization extinction ratio as functions of the gold film thickness and aperture width. Here, the relative efficiency is defined as the energy of the desired pattern divided by the total energy passing through the metasurface, and the polarization extinction ratio (ER) is defined as,

$$ER = 10 \log\left(\frac{T_{LCP(right)}}{T_{RCP(right)}}\right), \tag{5}$$

where $T_{LCP(right)}$ and $T_{RCP(right)}$ are the transmittances for LCP and RCP light at the right side. The details of simulation settings can be found in the ESI.† In Fig. 2c and d, all the results within the dashed line region can produce a polarization extinction ratio above 30 dB and a relative efficiency above 50%. Considering the performance and the fabrication condition of the metasurface, the final structural parameters for the experiment were set to: P_x = 0.896 μm, P_y = 0.45 μm, r = 0.37 μm, w = 0.07 μm, and d = 0.1 μm. In accordance with the detour phase effect, the output deflection angle of light is set to 45° in both the left and right sides at the wavelength of 633 nm.

4. Results and discussion

To experimentally verify the effectiveness of our designed metasurface, we build an experimental system (Fig. 3a). The incident laser beam is first collimated and expanded using two lenses (L1 and L2), and then converted to linear polarization using a polarizer (P1). The devices shown in dashed box 1 (Fig. 3a) are used to generate a circularly polarized OV beam, where a quarter waveplate is used to obtain circular polarization, and the 1st-order vortex waveplate (Thorlabs, WPV10L-633) converts the circularly polarized Gaussian beam into an OV beam with topological charge l = +1 or −1 through the normal or reversed direction of the vortex waveplate. The
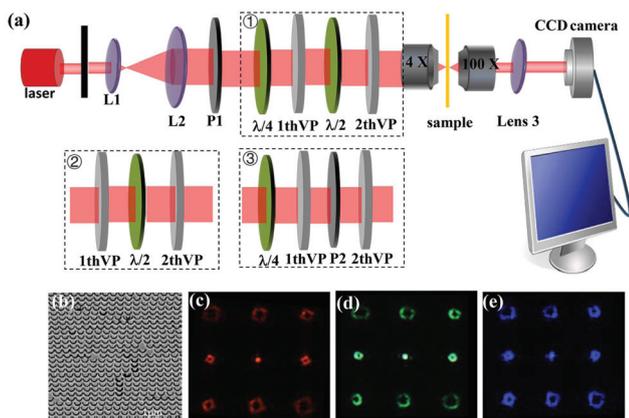
Fig. 3 (a) Illustration of the experimental setup. The dotted boxes labelled 1, 2, and 3 combined with the rest of the optical elements are used to generate the OV, CVB, and CVVB, respectively. (b) SEM image of the part of the metasurface fabricated by the FIB method. (c)–(e) are experimental results of the generated OV array for incident wavelengths of 473 nm, 532 nm, and 633 nm, respectively. The incident light is a left circularly polarized Gaussian beam, and the OV array is generated on the right side of the far field.

next half wave plate and the 2nd-order vortex waveplate (Thorlabs, WPV10-633) in dashed box 1 (Fig. 3a) can extend the OV topological charge to $l = +3$ or $−3$, or using only the quarter waveplate and the 2nd-order vortex waveplate to achieve $l = +2$ or $−2$. Therefore, a circularly polarized OV beam with OAM ranging from $l = −3$ to $+3$ can be generated. The devices in dashed box 2 (Fig. 3a) are used to generate a plane-wave CVB with polarization order $m = −3$ to $m = +3$. A CVVB can be generated using the devices in dashed box 3 (Fig. 3a), where the quarter waveplate combined with the 1st-order vortex waveplate are used to generate a circular polarized OV beam with $l = +1$ or $−1$, and the second polarizer (P2) is used to change the OV beam to a linear polarized light. The linear polarized OV beam then passes through the 2nd-order vortex waveplate and becomes a CVVB with both topological charges ranging from $l = −1$ to $+1$ and the polarization order ranging from $m = −2$ to $m = +2$. If more half waveplates and vortex waveplates are used, the range of the generated CVB and OV can be further extended.[42,43] With this method, we can experimentally generate light beams with a phase or polarization singularity or even both. The generated singular optical beams were focused using a 4× objective lens onto the fabricated metasurface sample. Finally, the far-field OV array patterns in both left and right sides were received using a 100× objective lens, and recorded using a CCD for the detection of the phase and polarization singularities.

Fig. 3b gives a scanning electron microscopy (SEM) image of the metasurface fabricated by the focused ion beam (FIB) method. The total area of the metasurface is $100 \times 100 \ \mu m^2$ on a gold film; the structural parameters are the same as introduced in the section above. To demonstrate the broadband features of the metasurface sample, in the experimental system, three different incident wavelengths of 473 nm, 532 nm, and

633 nm were chosen. In Fig. 3c–e, we show the experimental results of the generated far-field OV array on the right side under the illumination of a LCP Gaussian beam ($l = 0$) for the three stipulated wavelengths. The diffraction angles of these three wavelengths are 32°, 36°, and 45°, which are decided using the equation $\theta = \arcsin(\lambda/P)$ according to detour phase theory. Benefitting from this, this metasurface is able to detect the wavelength and OAM simultaneous,[44] when the sizes of OV arrays are carefully designed to avoid overlapping between adjacent wavelengths. Moreover, the generated OV arrays are always clear and give the desired OAMs (Fig. 2b), demonstrating the effectiveness and broadband performance of the metasurface.

Fig. 4 shows both FDTD simulated and experimental results of the phase singularity detection for different OV beams. The method of generating OAM, CVB and CVVB in simulation can be found in the ESI.† First, a LCP OV beam with $l = 1$ is incident on the metasurface; its spiral phase profile and donut-shaped intensity distribution are shown in Fig. 4a and b, respectively. From the spin-multiplexing and hologram functions of the designed metasurface, the transmitted beam propagates to the right side in the far field and forms an OV array with a restored Gaussian point at the position of $l_0 = −1$. Fig. 4c and d show the corresponding simulated and experimental results, respectively, both presenting a Gaussian point
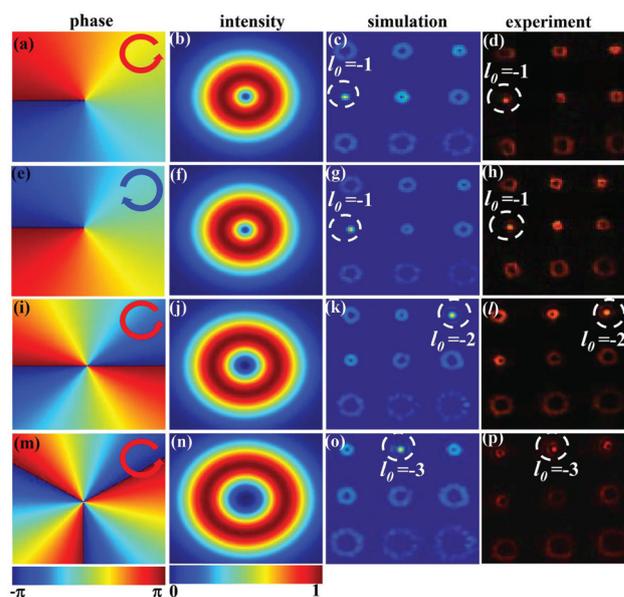

Fig. 4 FDTD simulated and experimental results in detecting the phase singularity of OV beams at 633 nm: (a)–(d) the incident phase distribution, the incident intensity distribution, the FDTD simulation result, and the experimental result at the right side of the far field, under the incidence of a left circularly polarized OV beam with $l = 1$. The Gaussian point (indicated by the white dashed circle) appears at the position of $l_0 = −1$ on the right-side OV array both in simulation and experiment. (e)–(h) are similar instances of (a)–(d) but under the incident right circularly polarized OV beam and show the OV array at the left side of the far field. (i)–(l) are similar instances of (a)–(d) but with topological charge $l = 2$. (m)–(p) are similar instances of (a)–(d) but with topological charge $l = 3$.

at the position of $l_0 = -1$. Fig. 4e–h show similar instances to those of Fig. 4a–d but with a RCP OV beam. Hence, the transmitted beam propagates to the left side, and the Gaussian point also appears at the position of $l_0 = -1$ in both simulated and experimental results. Comparing the two instances, the proposed metasurface simultaneously detects the OAM and SAM of the incident light depending on the position of the Gaussian point in the OV array and on the left/right side of the far field. The third row of the results in Fig. 4 shows instances of left circularly polarized OV beam with $l = 2$, the spiral phase profile of which exhibits a 4π phase change along the azimuthal direction in Fig. 4i. Its donut-shaped intensity distribution is given in Fig. 4j; the radius is also larger than that in Fig. 4b. A restored Gaussian point in the position $l_0 = -2$ of the original OV array is clearly seen on the right side of the far field in both simulated and experimental results (Fig. 4k and l). The fourth row of the results in Fig. 4 shows instances of the LCP OV beam with $l = 3$, with the phase profile appearing with a 6π phase change along the azimuthal direction (Fig. 4m). Its donut-shaped intensity distribution in Fig. 4n gives a larger radius than for $l = 2$ (Fig. 4j). The corresponding Gaussian point appears at position $l_0 = -3$ of the original OV array in both the simulated and experimental results (Fig. 4o and p), respectively. The results of Fig. 4 demonstrate that the proposed metasurface can be used to detect the phase singularity of OV beams efficiently.

Although in Fig. 4 we only demonstrate the detection of OV beams with $l = 1$ to 3, this metasurface device can detect OV beams ranging from $l = -4$ to $+4$ based on the 3×3 OV array, and more topological charges of OV can be detected by larger OV arrays through the design of the DOVG. For example, 25 different OAMs were detected through a 7×7 OV array in previous work.[45] Furthermore, it is demonstrated that our metasurface has potential applications in detecting fractional OAMs. Since the OV with fractional OAMs can be approximated as a linear combination of the two adjacent integer topological charges,[46] here we find that the fractional OAM could also be detected in our system by extracting the intensity value of the quasi-Gaussian points corresponding to adjacent integer topological charges, similar to our previous work.[47] The simulation results of the LCP OV beam with $l = 1.5$ and 2.5 can be found in ESI Fig. S3.†

Fig. 5 shows the results of polarization singularity detection for different CVBs. First, a CVB with polarization order $m = 1$ is the incident light on the metasurface and can be decomposed into a right circularly polarized OV with $l = 1$ and a left circularly polarized OV with $l = -1$, in accordance with eqn (2). Here, we choose $\varphi_0 = 0$, so its polarization state is actually a pure radial polarization (Fig. 5a). Based on the above-mentioned detection principle for the polarization singularity of a CVB, the transmitted beam through the metasurface propagates to both sides of the far field, where the restored Gaussian point appears at the position of $l_0 = -1$ on the left-side of the OV array and the position of $l_0 = 1$ on the right-side of the OV array. Fig. 5b and c show the simulated results, and Fig. 5d and e are the corresponding experimental results,
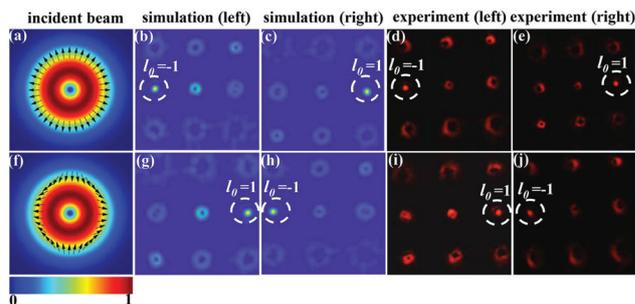

Fig. 5 Simulated and experimental results of detecting polarization singularity of CVBs at 633 nm. (a)–(e) are respectively the incident polarization distribution with the background of intensity distribution, the FDTD simulated results of the left- and right-side far field, the experimental results of the left- and right-side far field, under the incidence of a CVB with $m = 1$ and $\phi_0 = 0$. The Gaussian point (indicated by a white dashed circle) appears at the position of $l_0 = -1$ on the left-side OV array and at the position of $l_0 = 1$ on the right-side OV array in both simulation and experiment. (f)–(j) are similar instances of (a)–(e) but under the incidence of a CVB with $m = -1$.

which agree well with the simulated results. Another instance of CVBs with $m = -1$ is presented in Fig. 5f–j, which show the opposite situation to the first instance with $m = 1$. Its polarization state contains both radial and azimuthal polarization components (Fig. 5f). Fig. 5g–j give both the simulated and experimental results, demonstrating the Gaussian point at the position of $l_0 = 1$ on the left side and $l_0 = -1$ on the right side, with good agreement between the simulated and experimental results. The results in Fig. 5 verify that the proposed metasurface can serve as an efficient polarization singularity detector. The detecting range of the polarization order m for CVBs can also be extended by generating a larger OV array with more topological charges.

Finally, the detection of the CVVB with both polarization and phase singularities are studied in Fig. 6. The incident light is a CVVB with $l = 1$, $m = 2$, and $\varphi_0 = 0$, for which the Jones vector can be expressed as $J_{1,2} = \frac{1}{2} e^{i(3\varphi + \phi_0)} \binom{1}{-i} + \frac{1}{2} e^{-i(\varphi + \phi_0)} \binom{1}{i}$ in accordance with
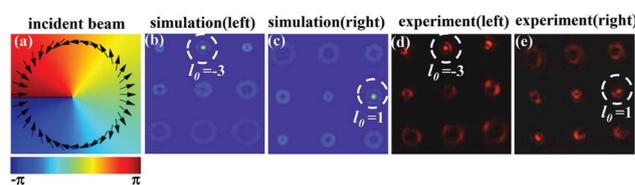

Fig. 6 Simulated and experimental results from the detection of both phase and polarization singularities of a CVVB at 633 nm. (a)–(e) are respectively the phase distribution and polarization distribution indicated by black arrows, the FDTD simulated results from the left- and right-side far field, and the experimental results of left- and right-side far fields, under the incidence of a CVVB with $l = 1$, $m = 2$. The Gaussian point (indicated by the white dashed circle) appears at the position of $l_0 = -3$ on the left-side of the OV array and at the position of $l_0 = 1$ on the right-side of the OV array in simulation and experiment.

eqn (3). Therefore, the CVVB can be decomposed into a RCP OV with topological charge $l = 3$ and a LCP OV with $l = -1$. The polarization state and helix phase distribution of the incident CVVB are shown in Fig. 6a. From the introduced detection principle of the CVVB, the Gaussian point appears at the position of $l_0 = -3$ on the left side of the OV array and $l_0 = 1$ on the right side of the OV array, respectively. Fig. 6b–e present both the simulated and the experimental results, respectively. It shows that Gaussian points appearing in the position of $l_0 = -3$ on the left side and $l_0 = 1$ on the right side, both in experiment and theoretical expectation. The results demonstrate that the proposed method can detect both phase and polarization singularities simultaneously.

As a matter of fact, the exact transmittance of our transmission-type plasmonic metasurface is not high (~4%), and the diffraction efficiency (defined as the ratio of desired pattern energy to total incident energy) is 2.1% under these experimental parameters ($P_x = 0.896$ μm, $P_y = 0.45$ μm, $r = 0.37$ μm, $w = 0.07$ μm, and $d = 0.1$ μm). Nevertheless, the transmittance, as well as the diffraction efficiency and energy utilization rate, can be improved using the Huygens metasurface[48] or using low-loss dielectric materials as references.[49–51] Meanwhile, the diffraction efficiency can be further improved by the optimization algorithm.[52] In the visible band, when the metal thickness reaches a certain level, the metasurface structure has a high reflectivity. Therefore, the sandwich structure of three layers, namely the metal plate at the bottom, the medium layer in the middle and the pattern at the top, can be designed to achieve the function of the metasurface and achieve a high energy utilization rate at the same time.[53] It is possible to make this metasurface tunable if phase change materials are employed,[54] and the method we demonstrated can also be applied in fiber communications when the structure is designed on the fiber end face, to realize an integrated detection device on the optical fiber.[55,56]

5. Conclusions

In conclusion, we propose and demonstrate a new method for detecting phase and polarization singularities simultaneously both in theories and experiments, based on a single spin-multiplexing metasurface. We designed, fabricated, and characterized a metasurface composed of a plasmonic semi-circular aperture array with a detour phase distribution on a metal film. Our experimental results agree well with the theoretical predictions, proving that the proposed method is successful in the detection of both the phase and polarization singularities. Moreover, three different wavelengths (473 nm, 532 nm, and 633 nm) were chosen in the experiment to demonstrate its broadband response feature. We believe that the proposed method for detecting phase and polarization singularities has great expectations in a variety of application fields, such as chip-level beam detection and high-capacity singularity-beam-multiplexing communications.

Conflicts of interest

There are no conflicts to declare.

References

1 M. S. Soskin and M. V. Vasnetsov, *Prog. Opt.*, 2001, **42**, 219–276.
2 M. R. Dennis, K. O'Holleran and M. J. Padgett, *Prog. Opt.*, 2009, **53**, 293–363.
3 S. W. Hell, Far-field optical nanoscopy, *Science*, 2007, **316**, 1153–1158.
4 M. F. Andersen, C. Ryu, P. Cladé, V. Natarajan, A. Vaziri, K. Helmerson and W. D. Phillips, *Phys. Rev. Lett.*, 2006, **97**, 170406.
5 S. Feng and P. Kumar, *Phys. Rev. Lett.*, 2008, **101**, 163602.
6 D. G. Grier, A revolution in optical manipulation, *Nature*, 2003, **424**, 810–816.
7 C.-L. Zhang, R. Wang, C.-J. Min, S.-W. Zhu and X.-C. Yuan, *Appl. Phys. Lett.*, 2013, **102**, 011114.
8 J. Leach, B. Jack, J. Romero, A. K. Jha, A. M. Yao and S. Frankearnold, *Science*, 2010, **329**, 662–665.
9 A. Mair, A. Vaziri, G. Weihs and A. Zeilinger, *Nature*, 2001, **412**, 313–316.
10 J. Wang, J. Y. Yang, I. M. Fazal, N. Ahmed, Y. Yan, H. Huang, Y.-X. Ren, Y. Yue, S. Dolinar, M. Tur and A. E. Willner, *Nat. Photonics*, 2012, **6**, 488–496.
11 N. Bozinovic, Y. Yue, Y. Ren, M. Tur, P. Kristensen, H. Huang, A. E. Willner and S. Ramachandran, *Science*, 2013, **340**, 1545–1548.
12 J. F. Nye and M. V. Berry, *Proc. R. Soc. London, Ser. A*, 1974, **336**, 165–190.
13 L. Allen, M. W. Beijersbergen, R. J. C. Spreeuw and J. P. Woerdman, *Phys. Rev. A*, 1992, **45**, 8185–8189.
14 T. Lei, M. Zhang, Y. Li, P. Jia, G. N. Liu, X.-P. Xu, Z.-H. Li, C.-J. Min, J. Lin, C.-Y. Yu, H.-B. Niu and X.-C. Yuan, *Light: Sci. Appl.*, 2015, **4**, e257.
15 M. Padgett and R. Bowman, *Nat. Photonics*, 2011, **5**, 343–348.
16 C.-L. Zhang, C.-J. Min, L.-P. Du and X.-C. Yuan, *Appl. Phys. Lett.*, 2016, **108**, 201601.

17 Q. W. Zhan, *Adv. Opt. Photonics*, 2009, **1**, 1–57.

18 Z.-K. Shao, J.-B. Zhu, Y.-F. Zhang, Y.-J. Chen and S.-Y. Yu, *Opt. Lett.*, 2018, **43**, 1263–1266.

19 R. Dorn, S. Quabis and G. Leuchs, *Phys. Rev. Lett.*, 2003, **91**, 233901.

20 H. Wang, L. Shi, B. Lukyanchuk, C. Sheppard and C. T. Chong, *Nat. Photonics*, 2008, **2**, 501.

21 M. Q. Cai, C. H. Tu, H. H. Zhang, S. X. Qian, K. Lou, Y. N. Li and H. T. Wang, *Opt. Express*, 2013, **21**, 31469–31482.

22 K. Y. Bliokh, F. J. Rodríguez-Fortuño, F. Nori and A. V. Zayats, *Nat. Photonics*, 2015, **9**, 796–808.

23 Y. Zhao and J. Wang, *Opt. Lett.*, 2015, **40**, 4843–4846.

24 V. Parigi, V. D'Ambrosio, C. Arnold, L. Marrucci, F. Sciarrino and J. Laurat, *Nat. Commun.*, 2015, **6**, 7706.

25 M. S. Soskin, V. N. Gorshkov and M. V. Vasnetsov, *Phys. Rev. A*, 1997, **56**, 4064–4075.

26 G. G. Liu, K. Wang, Y. H. Lee, D. Wang, P. P. Li, F.-W. Gou, Y.-N. Li, C.-H. Tu, S. T. Wu and H. T. Wang, *Opt. Lett.*, 2018, **43**, 823.

27 I. Moreno, J. A. Davis, I. Ruiz and D. M. Cottrell, *Opt. Express*, 2010, **18**, 7173.

28 N.-F. Yu, P. Genevet, M. A. Kats, F. Aieta, J.-P. Tetienne, F. Capasso and Z. Gaburro, *Science*, 2011, **334**, 333–337.

29 X.-J. Huang, H.-L. Yang, D.-H. Zhang and Y. Luo, *IEEE Trans. Antennas Propag.*, 2019, **67**, 4636–4641.

30 K. Ou, G.-H. Li, T.-X. Li, H. Yang, F.-L. Yu, J. Chen, Z.-Y. Zhao, G.-T. Cao, X.-S. Chen and W. Lua, *Nanoscale*, 2018, **10**, 19154.

31 X.-L. Chen, H.-L. Zhou, M. Liu and J.-J. Dong, *IEEE Photonics J.*, 2016, **8**, 4800308.

32 J.-C. Fang, Z.-W. Xie, T. Lei, C.-J. Min, L.-P. Du, Z.-H. Li and X.-C. Yuan, *ACS Photonics*, 2018, **5**, 3478–3484.

33 N. Zhang, X. C. Yuan and R. E. Burge, *Opt. Lett.*, 2010, **35**, 3495–3497.

34 S.-C. Gao, T. Lei, Y.-J. Li, Y.-S. Yuan, Z.-W. Xie, Z.-H. Li and X.-C. Yuan, *Opt. Express*, 2016, **24**, 21642–21651.

35 W. Ye, F. Zeuner, X. Li, B. Reineke, S. He, C. W. Qiu, J. Liu, Y. Wang, S. Zhang and T. Zentgraf, *Nat. Commun.*, 2016, **7**, 11930.

36 K. Y. Bliokh, Y. Gorodetski, V. Kleiner and E. Hasman, *Phys. Rev. Lett.*, 2008, **101**, 030404.

37 G.-X. Li, L. Wu, K. F. Li, S.-M. Chen, C. Schlickriede, Z.-J. Xu, S.-Y. Huang, W.-D. Li, Y.-J. Liu, E. Y. B. Pun, T. Zentgraf, K. W. Cheah, Y. Luo and S. Zhang, *Nano Lett.*, 2017, **17**, 7974–7979.

38 C.-J. Min, J.-P. Liu, T. Lei, G.-Y. Si, Z.-W. Xie, J. Lin, L.-P. Du and X.-C. Yuan, *Laser Photonics Rev.*, 2016, **10**, 978–985.

39 M. Khorasaninejad, A. Ambrosio, P. Kanhaiya and F. Capasso, *Sci. Adv.*, 2016, **2**, e1501258.

40 Z.-L. Deng, J.-H. Deng, X. Zhuang, S. Wang, K.-F. Li, Y. Wang, Y.-H. Chi, X. Ye, J. Xu, G.-P. Wang, R.-K. Zhao, X.-L. Wang, Y.-Y. Cao, X. Cheng, G.-X. Li and X.-P. Li, *Nano Lett.*, 2018, **18**, 2885–2892.

41 R. W. Gerchberg and W. O. Saxton, *Optik*, 1971, **35**, 237–246.

42 X.-Y. Weng, L.-P. Du, A.-P. Yang, C.-J. Min and X.-C. Yuan, *IEEE Photonics J.*, 2017, **9**, 6100208.

43 J. Bu, L.-C. Zhang, X.-J. Dou, Y. Yang, Y.-Q. Zhang and C.-J. Min, *Infrared Laser Eng.*, 2017, **46**, 0634001.

44 Y. Li, X. Li, L.-W. Chen, M.-B. Pu, J.-J. Jin, M.-H. Hong and X.-G. Luo, *Adv. Opt. Mater.*, 2017, **5**, 1600502.

45 T. Lei, S.-C. Gao, Z.-H. Li, Y.-S. Yuan, Y.-J. Li, M. Zhang, G. N. Liu, X.-G. Xu, J.-D. Tian and X.-C. Yuan, *IEEE Photonics J.*, 2017, **9**, 7901409.

46 M. V. Berry, *J. Opt. A: Pure Appl. Opt.*, 2004, **6**, 259–268.

47 N. Zhang, J. A. Davis, L. Moreno, J. Lin, K.-J. Moh, D. M. Cottrell and X.-C. Yuan, *Appl. Opt.*, 2010, **49**, 2456–2462.

48 R.-Q. Zhao, Z. Zhu, G.-H. Dong, T.-T. Lv, Y.-X. Li, C.-Y. Guan, J.-H. Shi and H. Zhang, *Opt. Lett.*, 2019, **44**, 3482–3485.

49 D.-P. Wang, Y. Hwang, Y.-M. Dai, G.-Y. Si, S.-B. Wei, D.-Y. Choi, D. E. Gómez, A. Mitchell, J. Lin and X.-C. Yuan, *Small*, 2019, **15**, 1900483.

50 L. Yang, D. Wu, Y.-M. Liu, C. Liu, Z.-H. Xu, H. Li, Z.-Y. Yu, L. Yu and H. Ye, *Photonics Res.*, 2018, **6**, 517–524.

51 D. Lin, P. Fan, E. Hasman and M. Brongersma, *Science*, 2014, **345**, 298–302.

52 Y. Li and M.-H. Hong, *Materials*, 2019, **12**, 1005.

53 G. Zheng, H. Mühlenbernd, M. Kenney, G. Li, T. Zentgraf and S. Zhang, *Nat. Nanotechnol.*, 2015, **10**, 308–312.

54 A. Nemati, Q. Wang, M.-H. Hong and J.-H. Teng, *Opto-Electron. Adv.*, 2018, **1**, 180009.

55 Z.-W. Xie, S.-C. Gao, T. Lei, S.-F. Feng, Y. Zhang, F. Li, J.-B. Zhang, Z.-H. Li and X.-C. Yuan, *Photonics Res.*, 2018, **6**, 743–749.

56 R.-S. Chen, J.-H. Wang, X.-Q. Zhang, J.-N. Yao, H. Ming and A.-T. Wang, *Opto-Electron. Adv.*, 2018, **1**, 180003.